



## OPEN Preclinical evaluation of polymer encapsulated carbon-based nano and microparticles for sentinel lymph node tattooing

Marta Baselga<sup>1</sup>, Antonio Güemes<sup>1,2</sup>, Manuel Arruebo<sup>1,3,4</sup>, Cristina Yus<sup>1,3,4</sup>, Teresa Alejo<sup>1,3,4</sup>, Víctor Sebastián<sup>1,3,4,5</sup>, Gema Martínez<sup>1,3,4,5</sup>, Dolores Arribas<sup>1,2</sup>, Gracia Mendoza<sup>1</sup>, Concepción Junquera<sup>1,6</sup> & Eva Monleón<sup>1,6,7</sup>

Selective sentinel lymph node biopsy (SNLB) is the standard method for detecting regional metastases in breast cancer patients. Identifying affected axillary lymph nodes before neoadjuvant treatment is crucial, as such treatment may alter drainage pathways and lymph node morphology, hindering the identification of sentinel lymph nodes. The use of carbon-based tattooing on sentinel lymph nodes (SLN) has been employed as a permanent tattooing method in clinical studies of Targeted Axillary Dissection (TAD), aiding in the SLN identification during surgery. Our study introduces a new method of lymph node tattooing based on poly lactic-co-glycolic (PLGA) particles with encapsulated carbon. This strategy substantially improves tattooing efficiency over single carbon suspensions currently used in clinical studies. We synthesized and characterized carbon-loaded PLGA micro- and nanoparticles, experimentally assessing their biological impact on porcine lymph nodes. The effect of particles' size and concentration was evaluated over time (from 1 to 16 weeks). Light and electron microscopy studies were conducted to characterize the cellular effects induced by the presence of these particles. Our findings reveal that the diverse physicochemical parameters of the particles interact differently with the lymphatic tissue, influencing their biodistribution within the lymph nodes and the intensity of the inflammatory response.

**Keywords** Targeted-axillary dissection, Sentinel lymph node biopsy, Nanoparticles, Carbon, Ultrastructure, Breast cancer, Carbon-tattooing

### Abbreviations

AL	Axillary lymphadenectomy
ANOVA	Analysis of variance
BC	Breast cancer
C-NPs	Carbon nanoparticles
DCM	Dichloromethane
GMC	Giant multinucleated cells
NAT	Neoadjuvant therapy
PLGA	poly(lactic-co-glycolic acid)
SEM	Scanning electron microscopy
SLN	Sentinel lymph node
SLNB	Selective sentinel lymph node biopsy
TAD	Targeted axillary dissection
TEM	Transmission electron microscopy

<sup>1</sup>Institute for Health Research Aragon (IIS Aragón), Zaragoza 50009, Spain. <sup>2</sup>Department of Surgery, University of Zaragoza, Zaragoza 50009, Spain. <sup>3</sup>Instituto de Nanociencia y Materiales de Aragón (INMA), CSIC-University of Zaragoza, Zaragoza 50009, Spain. <sup>4</sup>Department of Chemical Engineering, University of Zaragoza, Campus Río Ebro, Zaragoza 50018, Spain. <sup>5</sup>Networking Res. Center in Biomaterials, Bioengineering and Nanomedicine (CIBERBBN), Instituto de 13 Salud Carlos III, Madrid 28029, Spain. <sup>6</sup>Department of Human Anatomy and Histology, University of Zaragoza, Zaragoza 50009, Spain. <sup>7</sup>Centro de Encefalopatías y Enfermedades Transmisibles Emergentes, University of Zaragoza, Zaragoza 50009, Spain. ✉email: cyargon@unizar.es

## TGA Thermogravimetric analysis

At the time of diagnosing all cases of breast cancer (BC), it is essential to determine whether the axillary nodes are affected by the tumor. The current standard procedure to avoid Axillary Lymphadenectomy (AL) and its significant sequelae is the selective sentinel lymph node biopsy (SLNB). According to the experience on sentinel nodes, if the sentinel node is not affected, the likelihood of another axillary lymph node being affected is remote. Therefore, SLNB is sufficient to ascertain the status of the axillary nodes<sup>1,2</sup>. Traditionally, it has been stated that if axillary involvement is confirmed by ultrasound and biopsy at the time of diagnosis, SLNB is contraindicated, and AL is deemed mandatory. However, this paradigm has shifted in recent years.

The administration of neoadjuvant therapy (NAT) can be so effective that it leads to the disappearance, even complete, of tumor cells in both the primary tumor and the axillary lymph nodes. Detecting the sentinel lymph node (SLN) in patients who have undergone NAT poses significant challenges, as the treatment can alter lymphatic drainage pathways. Consequently, the technique exhibits a superior percentage of false negatives, wherein the SLN may not show tumor cells, while other non-sentinel lymph nodes might. This has profound implications, as it may leave a chemoresistant tumor in the axilla and underestimate the lesion, potentially resulting in suboptimal treatment for the patient<sup>3–6</sup>. Furthermore, previously metastatic nodes may not coincide with the sentinel node due to the blockage of lymphatic circulation. To decrease the rate of false negatives compared to conventional SLNB, it becomes necessary to macroscopically identify the nodes previously affected.

The ACOSOG Z107<sup>3</sup>, SENTINA<sup>4</sup>, and SN FNAC<sup>5</sup> studies demonstrated that, under certain conditions, performing SLNB after NAT in patients with metastatic lymph nodes was feasible and safe. The difficulty lies in identifying nodes that, when metastasized, were easily visible by ultrasound. However, after NAT, they can become unrecognizable due to their reduced size and the absence of ultrasound signs of infiltration. To address this challenge, Targeted Axillary Dissection (TAD) was introduced, involving the preoperative placement of a metallic clip after NAT. Although TAD is a promising concept, the preoperative placement of the metallic clip is not straightforward and necessitates an X-ray for guiding lymph node removal<sup>7–9</sup>. To avoid these limitations, various techniques have been described, including magnetic seeds<sup>10,11</sup>, radioactive seeds<sup>12–14</sup>, radar reflectors<sup>15,16</sup>, and carbon-based tattoos<sup>17–26</sup>.

Carbon-based tattoos could serve as an alternative to the localization methods described above, since they are inert and can remain in the lymph nodes indefinitely, being easily visible at macroscopic level<sup>17</sup>. Carbon tattoos in the TAD technique have gained popularity in recent years. Carbon does not interfere with the pathological assessment of nodal tissue and provides a distinct macroscopic staining compared to the tissues of the organism, making it suitable for the proposed application<sup>20</sup>. Commercial charcoal-based suspensions in doses of 0.1–1 ml (carbon black 0.01–1%w/v) have been the most widely used in clinical and preclinical trials, reporting nodal detection rates after NAT of 60–95% and false negative rates of 9.1–22%<sup>17,18,20–22,24</sup>. However, its adherence to the receptor tissue is compromised by the low viscosity of the substance itself, leading to its predominant distribution in the cortex of the lymph node and the surrounding fatty tissue. This results in non-homogeneous staining, as well as undesired dissemination via the lymphatic pathway, occurring in approximately 18% of cases<sup>18,27</sup>.

The use of polymeric nanostructured systems for sustained, localized, and extended release of active principles has been widely adopted in clinical practice for various therapeutic purposes, improving conventional delivery approaches. In this study, we evaluate the *in vivo* response after the administration of novel biodegradable sustained-release polymeric systems with the aim of easily detect with the naked eye the tattooed nodes. An exhaustive histopathological study of the effect of these carriers on the lymphatic tissue was also performed.

The aim of the study is to develop a tattooing method for its potential use in metastasized axillary lymph nodes in patients suffering from advanced breast cancer. This procedure will be conducted before NAT, facilitating the detection of those tagged lymph nodes during subsequent surgeries. We synthesized poly(lactic-co-glycolic acid) (PLGA) nano- and micro-particles to encapsulate tiny carbon nanoparticles by various approaches. We experimentally analyzed the lymph node tattooing in a total of 7 pigs to study the biological behavior and tattooing efficiency over time of each type of particle. The effect of the inoculated particles over time (1, 2, 4, 6, and 16 weeks), concentration (10 or 20 mg/ml), and size (micro- and nanoparticles, denoted as CE and CS, respectively) was assessed through histological and ultrastructural studies.

## Materials and methods

### Synthesis, characterization and *in vitro* studies of micro- and nanoparticles

#### Materials

Poly(D, L-lactide-co-glycolide) (PLGA Resomer<sup>®</sup> RG504H) was purchased from Evonik Industries AG, Poly(ethylene glycol)-block -poly(propylene glycol)-block-poly(ethylene glycol) (Pluronic<sup>®</sup> F-68), chloroform (CHCl<sub>3</sub>), ethyl acetate, dichloromethane (DCM), and polyoxyethylenesorbitan monolaurate (Tween<sup>®</sup> 20) were purchased from Sigma Aldrich (Merck KGaA; Darmstadt, Germany). The synthesis of the Carbon nanoparticles (C-NPs) was carried out by laser pyrolysis technology at the Unit 9 of the ICTS NANBIOSIS. The continuous gas flow reactor system and experimental protocol have been described elsewhere<sup>28,29</sup>.

Human dermal fibroblasts (NHDF-Ad) were obtained from Lonza (Basel, Switzerland), J774A.1 mouse monocyte-macrophages ATCC-TIB-67<sup>™</sup> were acquired from LGC Standards (Barcelona, Spain) and human breast adenocarcinoma cell line MDA-MB-231 were kindly donated by Dr. Alberto Jiménez Schumacher (IIS Aragón). These cell lines were used to determine the subcytotoxic dose of the nanoparticles used.

#### Synthesis of nanoparticles with encapsulated carbon

To evaluate the biological behavior of two different particle sizes, approximately in the order of 100 nm and 1000 nm, it was considered the use of well-known particle production approaches: (1) emulsion-solvent

evaporation to produce submicrometric particles and (2) electro spraying to generate micrometric particles. The optimized protocols are briefly described below.

The previously described oil-in-water (o/w) single emulsion-solvent evaporation method<sup>30</sup> was used for the encapsulation of the previously prepared C-NPs in the PLGA nanoparticles (Fig. 1a). Briefly, the organic phase was composed of 10 mg/ml of PLGA and 30 mg/ml of surfactant (Pluronic F-68) dissolved in 5 ml of ethyl acetate containing 5 mg/ml of C-NPs previously prepared by laser pyrolysis. 10 ml of Milli-Q water were added as the aqueous phase. The emulsification of both immiscible phases (organic and aqueous) was performed by an ultrasonic sonotrode (Branson Digital 450 Sonicator) under 40% amplitude and for 25 s. The resulting emulsion was left to evaporate on a stirring plate at 600 rpm for 3 h to evaporate the organic solvent and precipitate the particles. The particles were washed and recovered by centrifuging for 15 min at 15 °C and 7500 rpm.

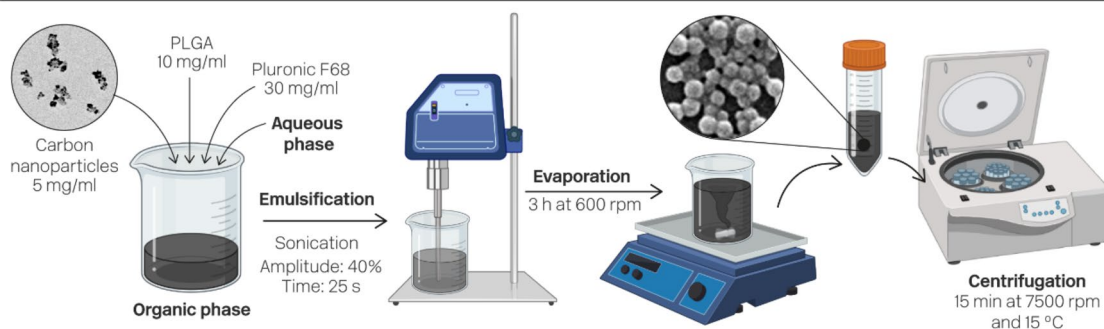
Microparticles were synthesized with an electro spinner (Yflow Electro spinner 2.2.D-500) using the uniaxial technique (Fig. 1b) following a previous protocol with some modifications<sup>31</sup>. Briefly, a solution of dichloromethane and chloroform was prepared (DCM: CHCl<sub>3</sub> (4:1)) containing 50 mg/ml of PLGA and 5 mg/ml of C-NPs previously prepared by laser pyrolysis, and stabilized with 10 mg/ml of Tween<sup>®</sup> 20. After optimization, a 15 cm distance between the collector and the needle and a dissolution flow rate of 0.5 ml/h were set. The Taylor cone was stabilized using a voltage of + 13 kV and - 3.9 kV corresponding to the tip of the needle and the collector plate, respectively. The synthesized materials were collected on aluminum foil, placed on a flat collector.

#### Preparation of tattooing vectors

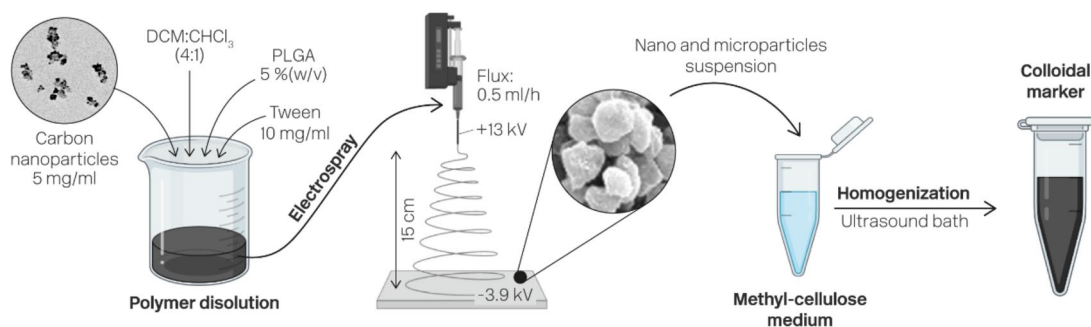
The synthesized nano- and microparticles were resuspended in a methylcellulose hydrogel for the preparation of injectable suspensions (Fig. 1c). The criterion for their optimization was to obtain sufficient viscous media to avoid the spread of the tag through the injection channel and in the tissue. The use of methylcellulose was chosen because it aids in the rheological stabilization of the administered suspension avoiding unwanted particle sedimentation, being suitable its use as an injectable<sup>32</sup>. Briefly, methyl cellulose was dissolved at a concentration of 1.0% (w/v) in water by alternately changing the temperature from 80 to 0 °C while the sample was subjected to magnetic stirring at 600 rpm. After optimization, the previously prepared carbon-encapsulated nano- and microparticles were resuspended at the selected concentrations (10 and 20 mg/ml) in 1.0% (w/v) methylcellulose.

As a result, 4 different vectors loaded with tiny C-NPs were obtained: CS10 (emulsified nanoparticles, at a concentration of 10 mg/ml), CS20 (emulsified nanoparticles, at 20 mg/ml), CE10 (electrosprayed microparticles, at 10 mg/ml) and CE20 (electrosprayed microparticles, at 20 mg/ml). Additionally, a non-encapsulated carbon nanoparticle suspension at 20 mg/ml was used as positive control (C-NPs).

#### (a) Emulsion method



#### (b) Electro spraying method



#### (c) Vector preparation

**Fig. 1.** Brief outline of the methods used for the synthesis and preparation of the vectors. (a) Emulsion-solvent evaporation method. (b) Electro spraying method. (c) Dispersion of the resulting vectors in methylcellulose medium.

### Scanning and transmission electron microscopy of nano- and microparticles

The morphological characterization and size distribution of the resulting particles were performed by scanning electron microscopy (SEM Inspect F50) at an acceleration voltage of 5–10 kV. The particles were prepared on carbon tape on an aluminum slide. The samples were coated with a Pd layer using a high vacuum coater (Leica EM ACE200, Wetzlar, Germany). Diameter distributions were obtained from manual measurements with the free Image-J software (v1.52; National Institutes of Health, 2019) for a sample of  $n = 100$ .

Particle morphology and dimensions were also characterized using a T20-*FEI* transmission electron microscope (*FEI* Company, Hillsboro, OR, USA) at 200 kV. TEM samples were prepared by depositing 50  $\mu\text{l}$  of the corresponding colloids dispersed in Milli-Q water on a formvar-coated copper grid and dried for at least 2 h.

### Quantification of encapsulated carbon

Quantification of the carbon encapsulated in the polymeric particles was performed by thermogravimetric analysis (Mettler Toledo TGA/STDA 851e, Mettler Toledo; Columbus, OH, US) using the degradation temperatures of the materials used during the emulsification and electrospaying ranging from 30 to 800 °C with a  $\text{N}_2$  flow rate of 50 ml/min. TGA was used as a quantification method of the different organic constitutive compounds as previously published<sup>33</sup>.

### Carbon release study

To obtain the carbon release profiles of the carbon-loaded nano- and microparticles, they were dispersed in distilled water (pH 7) and kept for 28 days at 37 °C under continuous agitation (~100 RPM). Aliquots of the supernatants were taken every day during the first week, and once a week for the rest of the month, i.e. on days 1, 2, 3, 4, 5, 6, 7, 14, 21 and 28. The amount of carbon released was quantified by UV-Vis spectroscopy (Jasco V670), with the maximum absorbance at 218 nm attributed to the electronic transition range of the carbon backbone from  $\pi$ - $\pi^*$ <sup>34</sup>.

### Cell viability assay

The cytotoxicity of the nanoparticles synthesized in this work was investigated using the Blue Cell Viability Assay (Abnova, Taiwan) according to the manufacturer's instructions<sup>35</sup>. Briefly, the cells were seeded at concentration of 6,000 cells/well for fibroblasts and J774A.1 cells and 18,000 cells/well for the MBA-MD-231 cell line and were incubated for 24 h at 37 °C and 5%  $\text{CO}_2$ . Subsequently, carbon nanoparticles (C-NPs), electrospayed carbon loaded microparticles (CE) and emulsified carbon loaded nanoparticles (CS) at different concentrations were added to the cells (0.1, 0.05, 0.025 and 0.01 mg/ml). After 24 h, the reagent (10% (v/v)) was added, cells were incubated for 4 h at 37 °C and 5%  $\text{CO}_2$  and fluorescence was read at 530/590 ex/em in a Varioskan LUX microplate reader (Thermo Fisher Scientific, Waltham, Massachusetts, U.S.). Cytotoxicity was evaluated by comparing the values obtained for the treated cells with the ones retrieved from untreated cells, considering these controls as 100% viability. Four replicas of each experiment were performed in triplicate. All results are presented as mean  $\pm$  standard deviation. Data were analyzed using two-way analysis of variance (ANOVA) (GraphPad Prism 8, San Diego, US). Statistically significant differences were considered when  $p \leq 0.05$ .

## In vivo studies

### White Landrace pigs

Seven female White Landrace pigs with an average weight of 25 kg (22–30 kg) from Inga Food SA (Madrid, Spain) were used. The experimental animals were divided into two study groups. The “short-term study” included 4 animals which were housed for 1, 2, 4 and 6 weeks, and the “long-term study” included 3 animals which were housed for 16 weeks. The study was carried out in the facilities of the Institute of Health Sciences (IIS Aragón, Spain), in accordance with the ARRIVE guidelines and the Spanish Policy for Animal Protection RD53/2013 which meets the European Union Directive 2010/63. The experimental procedure was approved by the Animal Research Ethics Committee of the University of Zaragoza under reference PI09/20.

### Surgical procedure, lymph node tattooing and sampling

In all animals, injections of the pigments were performed in the selected peritoneal lymph nodes from the splenic artery root, portal vein root and distal ileum regions. We initially aimed to label axillary nodes but due to the difficulty encountered during their ultrasound guided identification, due to the different consistency of porcine and human axillary tissues, we decided to perform direct punctures in mesenteric nodes (of similar size to those of humans). In each animal, 2–3 and 2–4 lymph nodes were tattooed per animal using both CE20 and CS20 vectors in the “short-term study” and the “long-term study” groups, respectively. In the “long-term study” group, 3 and 6 peritoneal lymph nodes were also tattooed with CS10 and CE10 vectors respectively to assess the effect of the particle's concentration. A control node using carbon nanoparticles (C-NPs) not encapsulated in the polymeric PLGA-based matrix was tattooed per experimental animal mimicking the conventional carbon-based pigments currently used in the clinic<sup>17,18,20–22,24</sup>. For vector administration surgery, a midline laparotomy was performed to expose the abdominal viscera and isolate the selected mesenteric nodes. Once exposed, the nodes were tattooed for subsequent identification using different silk stitch patterns. Vectors were loaded in 0.2 ml doses (10 or 20 mg/ml) into 1 ml syringes and 21G needles were attached. Direct puncture was performed in the lymph nodes of the splenic artery root, portal vein root and distal ileum. After surgery, the animals were housed in special conditions in heated cages. We used buprenorphine (Buprenodale, Dechra, 0.05–0.1 mg/kg/day) during the first 72 h after surgery, and antibiotic prophylaxis with enrofloxacin (Enroflox, Agrovit Market SA, 2.5 mg/kg) until lymph node dissection surgery performed after 1, 2, 4, 6, or 16 weeks. For lymph node dissection surgeries, a wide median laparotomy was also performed. Tattooed lymph nodes were identified

macroscopically by showing a dark pigmentation characteristic of the vector administered. The tattooed lymph nodes were resected next to the identification sites and separated for further processing.

#### Anesthesia and euthanasia

The surgical procedure was performed under general anesthesia with oral intubation, mechanical ventilation and neuromuscular blockade. Animals were premedicated with zolazepam (Zoletil, Virbac, 0.05 mg/kg) and intramuscular dexmedetomidine (Dexmopet, Fatro Iberica SL, 0.08 ml/kg). Anaesthetic induction was performed with disopropylphenol (Propofol 1% MCT, Fresenius Kabi Laboratories Spain, 6 mg/kg) and sevoflurane 1.9% (Baxter SL) was used for maintenance. Muscle block was induced with pancuronium bromide (Pavulon, Organon Española SA, 4 mg/ml). Intraoperative analgesia consisted on the continuous infusion of fentanyl (Fentanest, Aurovitas España, 10 µg/kg/h) and Ringer's lactate (8 ml/kg/h) was the solution used as fluid therapy. At the end of the experiment, the animals were euthanized by a single injection of potassium chloride (1 mEq/kg) intravenously, preventing depolarisation of the heart muscle and causing it to stop.

#### Macroscopic studies

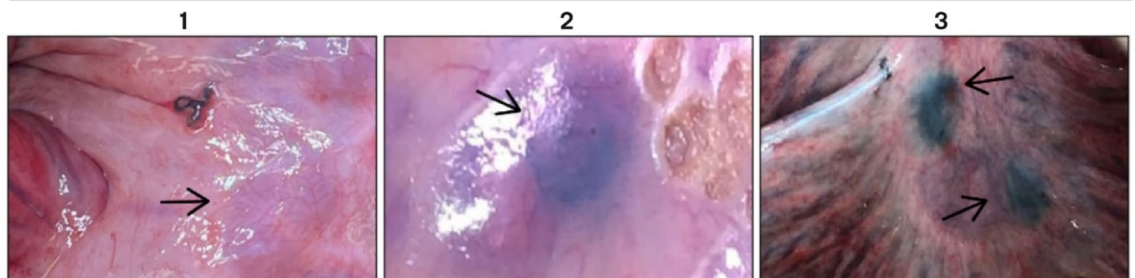
Before dissection surgery, the tattooed lymph nodes were photographed in situ and the ease of their visual identification was qualitatively scored on a scale from 1 to 3, with 1 being 'indistinguishable' (tagged with the silk stitch but no optical signal to the naked eye of the vector was present), 2 "moderate" (tagged with the silk stitch and having a moderate optical signal of the vector present) and 3 "optimal" (tagged with the silk stitch and having a clear optical signal attributed to the vector present) identification (Fig. 2a).

After sampling, lymph nodes were fixed in 4% formalin for 3–5 day. Lymph nodes were dissected away from the adjacent tissue and the largest tattooed side of the nodes was photographed. The photographs were used to calculate the percentage of the tattooed lymph node area based on a histogram analysis (Fig. 2b). The background of the image was colored white to subsequently remove these pixels and delimit the extent of the lymph node. The image was converted to greyscale and image correction parameters were manually adjusted to achieve an acceptable contrast between the untattooed lymph node tissue and the tattooed area. The histogram of the image was extracted using ImageJ software<sup>36</sup> and the percentage of the tattooed area was calculated by quantifying the number of pixels with the darkest 30% of greys, taking into account the entire pure non-white area. This system was validated by manually calculating the area of 3 lymph nodes. An error of  $\pm 3\%$  in the tattooed area selected was estimated calculating the total lymph node area and the area marked by manual segmentation using Gimp 2.10.38 software.

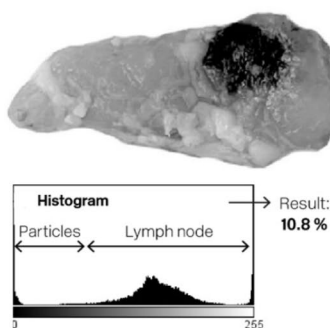
#### Microscopic studies

The formalin-fixed lymph nodes were cut into approximately 3 mm thick tissue slices and the most pigmented slice was selected for histological processing. Samples were processed according to standard procedures and

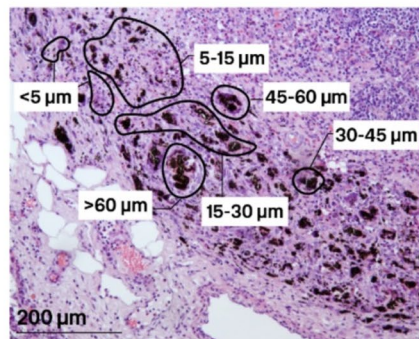
#### a. Ease of identification scale



#### b. Tattooed area



#### c. Clusters size



#### d. Extension of inflammation

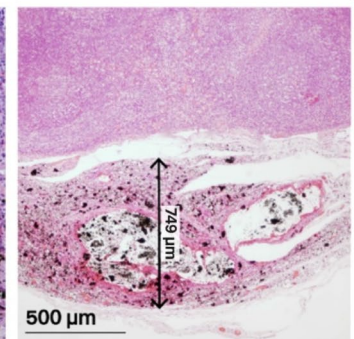


**Fig. 2.** Macroscopic variables analyzed: (a) Ease of identification scale. (b) Estimation of the tattooed nodal area. (c) Morphometry of the particles clusters. (d) Extension measurement of the inflammatory response.

stained with hematoxylin and eosin (H&E) for light microscopy examination. Histological processing and staining were carried out by the Scientific Technical Services - Microscopy and Pathology at IIS Aragón.

Histologic slides were evaluated by light microscopy to determine the presence and location of the pigment and to assess the histological changes after the administration of the different pigments. In addition, the size of clusters formed by particles agglomerates and the intensity of the histological changes were evaluated based on a histogram analysis.

The size of the clusters formed by the inoculated particles were measured from micrographs of each tissue section using ImageJ software<sup>36</sup> (Fig. 2c). Six size ranges were established: <5  $\mu\text{m}$ , 5–15  $\mu\text{m}$ , 15–30  $\mu\text{m}$ , 30–45  $\mu\text{m}$ , 45–60  $\mu\text{m}$  and > 60  $\mu\text{m}$ . A total of 50 clusters were counted in each tattooed node ( $n = 50$ ).

Finally, the degree of intensity of the inflammatory response was quantified according to the extent of the inflamed tissue. The most extensive section of inflammatory tissue in the lymph node was manually measured using ImageJ software<sup>36</sup> (Fig. 2d).

#### Ultrastructural studies

After sampling, biopsies were fixed in 2% glutaraldehyde in PB for 3 days and subsequently washed with PB. Samples were post-fixed with 2% osmium, rinsed, dehydrated in graded acetone (30%, 50%, 70% with 2% uranyl acetate, 90%, 100%), cleared in propylene oxide and embedded in araldite (Durcupan, Fluka AG; Buchs SG, Switzerland). An RMC MT-XL ultramicrotome was used for obtaining semi-fine and ultra-fine slices. Semi-thin (1.5  $\mu\text{m}$ ) and ultra-thin (0.05  $\mu\text{m}$ ) sections were cut with a diamond knife. Semi-thin sections were stained with 1% toluidine blue and examined by light microscopy (Olympus BX51 microscope, Olympus Imaging Corporation; Tokyo, Japan). Ultra-thin sections were collected on Formvar-coated single-slot grids counterstained with 1% uranyl acetate and Reynold's lead citrate staining. The samples were observed at the Electronic Microscopy Service of Biological Systems of the University of Zaragoza with a JEOL JEM 1010 transmission microscope operating at 80 kV.

#### Statistical analysis

Statistical analyses were performed with IBM SPSS Statistics (SPSS Inc.; Illinois, USA). C-NPs-tattooed lymph nodes were only used as control and were not included in the statistical studies. To study whether the data came from a normal population, they were analyzed using the Shapiro-Wilk test. The variable of tattooed area showed a normal distribution. According to that, the corresponding tattooed area was analyzed using the t-Student test and the remaining variables were assessed using nonparametric tests. Independent groups were then established according to time ("short-term study" (1–6 weeks) and "long-term study" (16 weeks) groups), type of tattooing (CS10, CE10, CS20 and CE20, considering only data from the "long-term study" group), concentration (CS10-CE10 and CS20-CE20, considering only data from the "long-term study" group), and particle size (CS10-CS20 and CE10-CE20). In these groups, the data analysis was performed using the Mann-Whitney U test. Significant differences were considered when  $p \leq 0.05$ . Correlation studies between variables used Kendall's rank correlation coefficient. Statistically significant correlations were considered when  $p \leq 0.05$ .

## Results

### Characterization of nano- and microparticles

The optimized particle morphology and size distribution histogram were characterized using scanning electron microscopy (Fig. 3a, g). Figure 3(m, n) depicts the morphology and size of the C-NPs here considered as a cargo in PLGA nano and microparticles. C-NPs have a mean particle size of  $12.4 \pm 3.1$  nm (Fig. 3o). An average nanoparticle size (emulsion, CS, Fig. 3b) of  $123 \pm 32$  nm was estimated, which increased to  $1.07 \pm 0.41$   $\mu\text{m}$  in the case of microparticles (electrospray, CE, Fig. 3h). The heterogeneity in particles size was determined with the polydispersity index (PDI), which was 0.07 for CS and 0.15 for CE, considering a PDI value lower than 0.25 as a narrow size distribution of the sample<sup>37,38</sup>. Therefore, the CE were more polydisperse in size than the CS. Transmission electron micrographs revealed the presence of carbon nanoparticles (dark contrast dots of approximately 12–20 nm) encapsulated inside the nano- and microparticles for both syntheses (Fig. 3c, i, respectively) although for the CE microparticles some C-NPs were localized not only in the core but also attached on the surface of the microparticles.

TGA analysis of the CS obtained by single emulsion-solvent evaporation revealed an average PLGA content of 87.5 wt% and an average carbon content of 12.5 wt% (Fig. 3d). The TGA curves indicate a remaining weight between 6.1 and 23.5 wt% (associated to carbon), so the carbon encapsulation performance results may be slightly underestimated. These results were similar to those of CE, with an average PLGA content of 86.7 wt% and carbon content of 12.3 wt% (Fig. 3j).

The carbon released in vitro was less than 1 wt% during the first month for both nano- and microparticles (Table 1; Fig. 3e, k). The reduced carbon release rate can be explained by (1) the large hydrophobicity of the carbon nanoparticles, which does not disperse or solubilize in water and were not released from the PLGA encapsulating mixed matrices and (2) because the particles to be released were large enough ( $12.4 \pm 3.1$  nm, Fig. 3o) and would require an extensive degradation of the PLGA-based polymeric matrix in order to be released. This represents a positive outcome considering that the longer the permanence of the carbon nanoparticles within the polymeric particles, the better the intensity of the tattooing. It is important to point out that according to the manufacturer the degradation timeframe of the PLGA used (PLGA Resomer<sup>®</sup> RG504H) is less than 3 months. The hydrolytic degradation of the polymer would initially produce a burst C-based nanoparticles initial release followed by a sustained release over time caused by its bulk erosion. As it is shown in Fig. 3e, k an initial burst release was not observed, probably due to the hydrophobic nature of the C-based nanoparticles, instead a lineal release was measured in vitro which would match a first order release kinetics, indicative of a concentration dependent

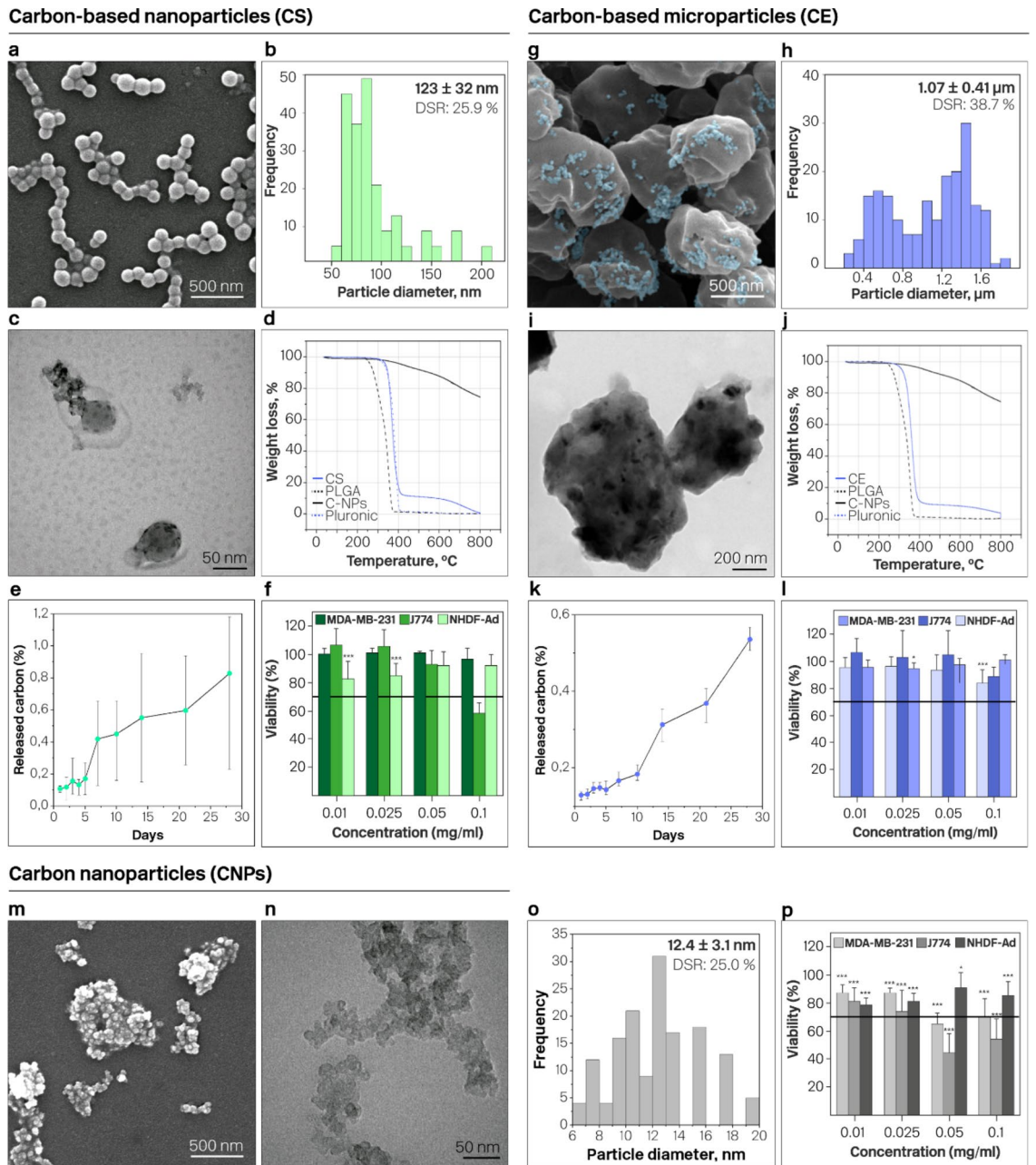


**Fig. 3.** Characterization of the polymeric particles containing C-NPs synthesized (a–f) by emulsion (CS) and (g–l) by electrospaying (CE), and (m–p) carbon nanoparticles (C-NPs). (a, g, m) Scanning electron micrographs of the particles. The carbon nanoparticles have been artificially coloured in blue to make them more visible in the micrographs. (b, h, o) Histograms of the size distributions. (c, i, n) Transmission electron micrographs of the particles, where carbon is clearly distinguished by its higher electron density. (d, j) Thermogravimetric curves. The solid blue line represents the mass loss of the micro and nanoparticles, the dashed black line represents the weight loss of empty PLGA, the solid black line represents the weight loss of carbon and the dashed blue line represents the weight loss of the stabilizer, in the case of the nanoparticles from the polymeric nano- and microparticles in PBS 1x medium. (e, k) Curves of the release kinetics of the encapsulated carbon nanoparticles from the polymeric nano- and microparticles in PBS 1x medium. (f, l, p) Cell viability in the fibroblast (NHDF-Ad), macrophages (J774), and human breast adenocarcinoma (MDA-MB-231) cell lines. Untreated control cells were assigned as 100% viability. Statistical analyses are referred to untreated control cells (\* $p < 0.05$ , \*\* $p < 0.01$ , \*\*\* $p < 0.001$ , \*\*\*\* $p < 0.0001$ ).

mechanism. Over time, the amount of C-based nanoparticles released would depend on the remaining amount of the particles entrapped in the mixed matrix.

The cytotoxic effects of the C-NPs, CE and CS are depicted in Fig. 3(f, l, p) compared with the untreated cells (100% viability). Following the recommendations of the ISO 10993-5 for medical devices, viability below 70% is

	Released carbon (wt%)			
	1 week	2 weeks	3 weeks	4 weeks
Carbon from Nanoparticles	0.42 ± 0.3	0.55 ± 0.6	0.59 ± 0.5	0.83 ± 0.5
Carbon from Microparticles	0.17 ± 0.0	0.31 ± 0.0	0.37 ± 0.0	0.53 ± 0.0

**Table 1.** Percentage of carbon released in vitro in nano and microparticles.

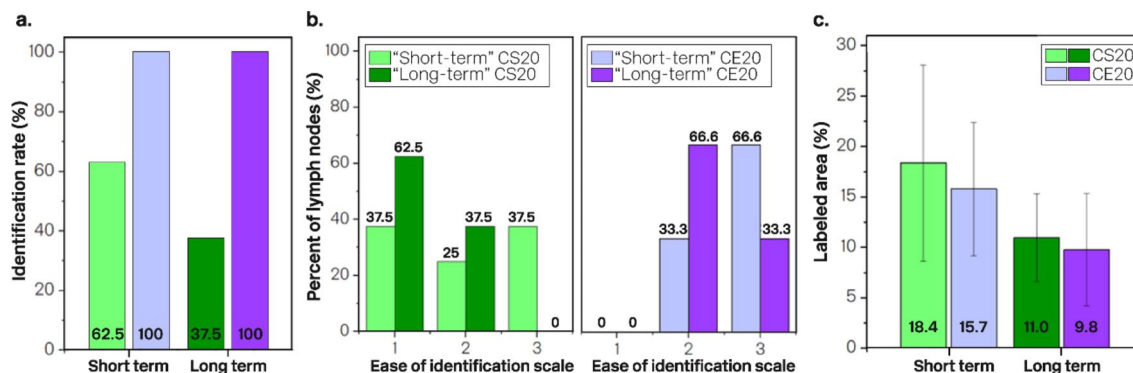


**Fig. 4.** Macroscopic and microscopic variables analyzed. (a) Identification rates of CE20 (colored in blue and purple) and CS20 (colored in shades of green) tattoos. (b) Frequency of dissected lymph nodes showing difficult (1), moderate (2) or easy (3) identification. (c) Percentage of tattooed area over time for CS20 and CE20 vectors.

considered cytotoxic<sup>39</sup>. Accordingly, no cytotoxic effect was observed for fibroblast and MDA-MB-231 cell lines for CE and CS particles at any of the concentrations assayed, yielding viability values higher than 75 and 95%, respectively. For macrophages a slight increase in the cytotoxicity was observed when cells were treated with CE at the higher doses assayed. When both, fibroblasts and MDA-MB-231, were treated with C-NPs no cytotoxic effect was observed but, conversely, high concentrations of C-NPs (0.05 and 0.1 mg/ml) exerted cytotoxicity for macrophages. These results revealed a significant reduction of the cytotoxicity when C-NPs were encapsulated in the polymeric NPs.

### Macroscopic studies

Both vectors studied were identifiable intraoperatively from 1 to 16 weeks after injection. CE20 tattooed lymph nodes were more easily identified than CS20 were ( $p=0.053$ ). Nodes with an “ease of identification” of 2 and 3, could be easily found during nodal resection surgery. However, nodes rated 1 did not show easily identifiable tattoos. Compared to the silk stitch label, 100% of the lymph nodes were tattooed when using the CE20 vector. In the case of the CS20 vector, 62.5 and 37% of the lymph nodes were tattooed in the “short-term” and “long-term” groups, respectively (Fig. 4a-b). The ease of identification decreased with statistical significance over time ( $p=0.005$ ). In the “long term” study, 42.9 and 25% of the lymph nodes were tattooed with CE10 and CS10 vectors, respectively. The results show that the increase of concentration in CE-tattooed nodes positively correlated with the ease of identification ( $p=0.02$ ). However, no correlation was found for the CS-tattooed nodes.

As expected, a significant positive correlation was found between the ease identification and the percentage area of the lymph nodes tattooed ( $p=0.003$ ). For both vectors, the percentage area of the lymph nodes tattooed was larger in the “short-term study” than in the “long-term study” group (Fig. 4c). The reduction of the tattooed area over time was statistically significant ( $p=0.014$ ). From the first to the 16th week, this reduction was ~2.2 and ~1.9 fold for CE20 ( $22.0 \pm 2.2\%$ ) and CS20 ( $20.5 \pm 11.4\%$ ), respectively. Additionally, the long-term study group showed a reduction in the percentage of tattooed area related to the decrease in particle concentration in the case of CS vectors (CS20  $11.0 \pm 4.4\%$  - CS10  $7.4 \pm 5.7\%$ ) but not in CE vectors (CE20  $9.9 \pm 5.6\%$  - CE10  $11.1 \pm 3.6\%$ ) (Figure S1).

In the C-NPs-tattooed lymph nodes (control) of “short-term study” group, 66.6% of lymph nodes were properly identified. Nevertheless, in the “long-term study” group, no lymph node was easily identified. In the “short-term study” group, C-NPs vectors tattooed the  $15.5 \pm 0.2\%$  of the surface, which was reduced to  $2.5 \pm 3.5\%$  in the “long-term study” group. This preliminary data suggests a ~6.2-fold reduction. Therefore, conventional carbon-based markers based on nanoparticles provided a reduced contrast in the tissue compared to our vectors that contain in the interior of a polymeric matrix those carbon nanoparticles. C-NPs (control) samples were not included in the statistical study since the number of lymph nodes obtained after this tattooing was reduced. However, we use these results descriptively in light and electron microscopy studies.

### Microscopic studies

Histopathologic evaluation of the lymph nodes revealed that CE20 and CS20 vectors were located mainly in the inner, in the pericapsular area or/and in the soft tissue adjacent to the node (Fig. 5a). The main location was pericapsular and/or adjacent in all cases (Fig. 5b).

The polymeric particles rearranged themselves into different microscopic structures, giving rise to clusters of varied dimensions. Clusters of 5 to 15  $\mu\text{m}$  were most frequently observed. In the “short-term study” group, average cluster sizes were  $14.5 \pm 4.0$  (CS20) and  $19.1 \pm 10.2$   $\mu\text{m}$  (CE20). In the “long-term study” group, clusters measured  $44.5 \pm 44.1$  (CS20),  $14.1 \pm 8.3$  (CE20),  $21.0 \pm 5.6$  (CS10),  $15.7 \pm 6.6$   $\mu\text{m}$  (CE10) (Fig. 5c). Although not statistically significant, a reduction in cluster size was observed as stabling time increased.

In all samples from the “short-term study”, a foreign body reaction associated with the presence of the pigments was observed. The inflammatory process was characterized by the presence of macrophages and giant multinucleated cells (GMC) that engulfed the particles since the first week. Extracellular particles were also present (Fig. 5e-g). Small foci of necrosis associated with foreign body reaction were observed occasionally for both vectors. CE vectors induced a larger inflammatory response than CS vectors did ( $p=0.029$ ). Additionally, the extent of the inflammatory response positively correlated with the tattooed area ( $p=0.051$ ). A statistically significant reduction in the intensity of the inflammation was observed over the weeks ( $p=0.04$ ). After 16 weeks of stabling, the presence of inflammation was substantially reduced and almost all lymph nodes showed mild or no inflammation. The reductions of the extension of the inflammatory tissue from the “short-term study” group to the “long-term study” group were from  $223 \pm 174$  to  $104 \pm 57$   $\mu\text{m}$  (CS20) and  $413 \pm 250$  to  $278 \pm 207$   $\mu\text{m}$  (CE20) (Fig. 5d). Thus,  $\sim 2.1$  and  $\sim 1.5$ -fold reductions were identified. A foreign body reaction associated with low particle concentration vectors was also observed. The inflammatory reaction was higher in the CE10 ( $239 \pm 151$   $\mu\text{m}$ ) than in CS10 vector ( $75 \pm 16$   $\mu\text{m}$ ) probably attributed to the larger sizes of the former.

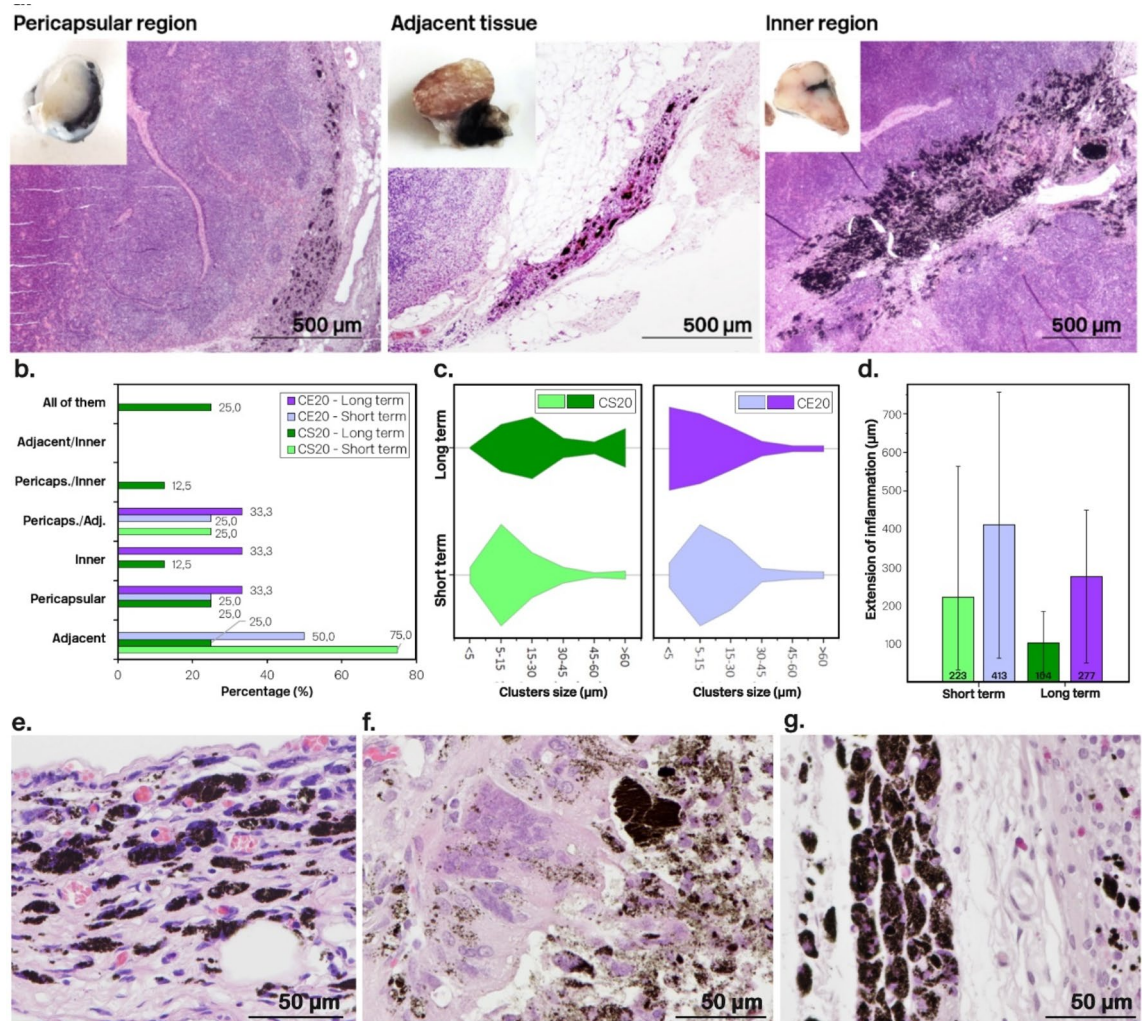


**Fig. 5.** (a) Particles localization in the three different nodal regions (pericapsular region, adjacent tissue and inner region). (b) Particle’s location in CS20 and CE20 tattooed nodes. (c) Clusters size in CS20 and CE20-tattooed nodes. (d) Extension of the inflammatory tissue in CS and CE20 tattooed nodes. (e–g) Inflammatory reaction associated with (e) CE20 and (f, g) CS20 vectors.

In C-NPs samples, samples at short times show the formation of large carbon clusters within the lymph node. In “short-term study” group, the average of cluster’s size was  $25.0 \pm 24.4 \mu\text{m}$ , while in the “long-term study” group was  $5.8 \pm 0.4 \mu\text{m}$ . There is a tendency for them to disintegrate into smaller, more dispersed clusters as the weeks go by. In nodes tattooed with C-NPs (control) inflammation was highly variable and reduced from  $541 \pm 245$  to  $14 \pm 19 \mu\text{m}$  (~40-fold reduction).

### Ultrastructural study

Inoculated particles were mainly found internalized in macrophages, isolated by or in the cytoplasm of GMC, or recruited into the connective tissue surrounding the lymph node.

In the early stages of the particle uptake process, in all cases macrophages internalize the particles through the formation of filopodia and lamellipodia (Fig. 6).

Macrophages phagocytosed all three types of particles. They are easily distinguished by their ultrastructural characteristics: carbon microparticles (CE) (Fig. 7a-b), carbon nanoparticles (CS) (Fig. 7c-d) and non-encapsulated carbon particles (C-NPs) (Fig. 7e-f). The average size of phagocytosed CE particles retrieved from the ultrastructural images is  $911.6 \pm 547.9 \text{ nm}$  ( $n=50$ ). CS particles show an average size of  $99.6 \pm 43.2 \text{ nm}$  ( $n=50$ ). Finally, C-NPs tend to aggregate into structures of  $41.9 \pm 16.6 \text{ nm}$  ( $n=50$ ). The phagolysosomes observed inside macrophages presented differences in size, morphology and electron density. The membrane of CE and CS loaded phagolysosomes is physically bounded to the surface of the microparticles, which generates regular and rounded morphologies (Fig. 7b-c). However, the morphology of C-NPs phagolysosomes is more irregular (Fig. 7e).

After particle uptake by macrophages (Fig. 8a), the carbon particles cause disruption of the phagolysosome membrane in all three cases (Fig. 8b-c). As a result of membrane rupture, the lysosomal hydrolases are released into the cytosol, which cause lysis of the cell membrane itself with subsequent release of the cell organelles into the extracellular space (Fig. 8d-e), with the carbon particles remaining intact (Fig. 8d).

Although the particles were mainly found in macrophages, particles were also observed in GMC which are formed by the fusion of macrophages and can isolate the pigments in the extracellular space or within the cytoplasm. (Fig. 9a).

The cellular debris and particles released by the rupture of the macrophage membranes are phagocytosed by new macrophages and so on. Thus, macrophages with numerous phagolysosomes with carbon in their interior were found (Fig. 9b). After 4 weeks, the polymer degraded, and more free carbon particles were found (Fig. 9b-d). Isolated high-carbon macrophages were observed within a matrix of collagen fibers in the adjacent tissue (Fig. 9d).

### Discussion

The tattooing of lymph nodes is increasingly employed in clinical trials to tattoo SLN in breast cancer patients before NAT. This strategy is low cost, does not require preoperative localization procedures and minimizes additional discomfort for the patient, making it promising for lymph node tattooing in oncologic patients<sup>40</sup>. Carbon-based tattoos are beginning to be validated in clinical studies<sup>17–26</sup>. In our experimental study, we have developed two carbon-based vectors based on C-NPs encapsulated within a biodegradable polymeric matrix and inoculated in pig lymph nodes. The identification rate (moderate-optimal visibility on the identification scale) in the “short-term study” group (1–6 weeks) was high in lymph nodes tattooed with both vectors (62.5–100%). In the “long-term study” group (16 weeks), the rates were lower (25.0–66.7%). Our results are in line with other clinical studies performed, which reported a positive identification rate of 69–100%<sup>18–25,41,42</sup>.

Lymph nodes tattooed with 0.2 ml of CE20 vectors were adequately identified in node resection surgeries. It was possible to identify 100% of the nodes in both the “Short-term study” and in the “Long-term study” groups.

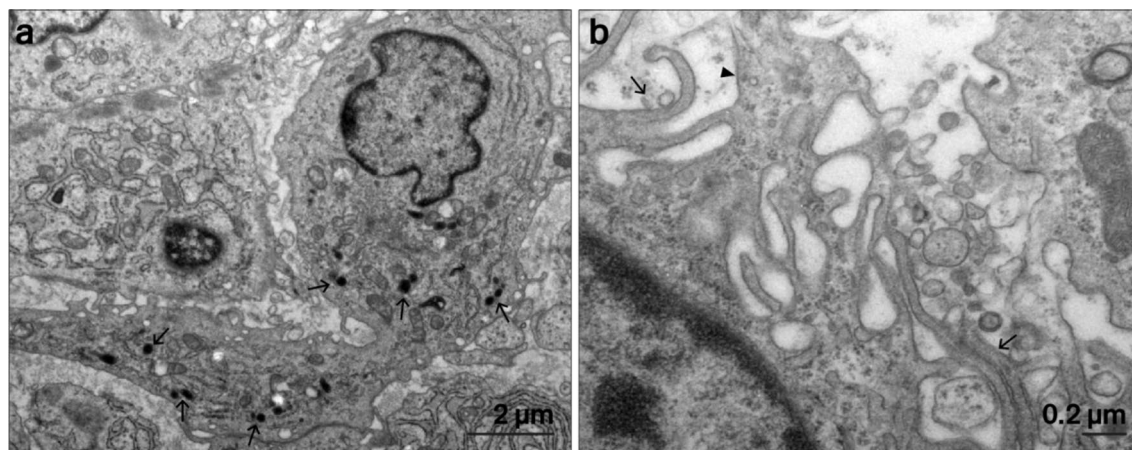


**Fig. 6.** Structure and ultrastructural features of macrophages. **(a)** Macrophage with numerous lysosomes (arrows) in its cytoplasm. **(b)** Lamellipodia (arrowhead) and filopodia (arrow) emerging from the surface of a macrophage.

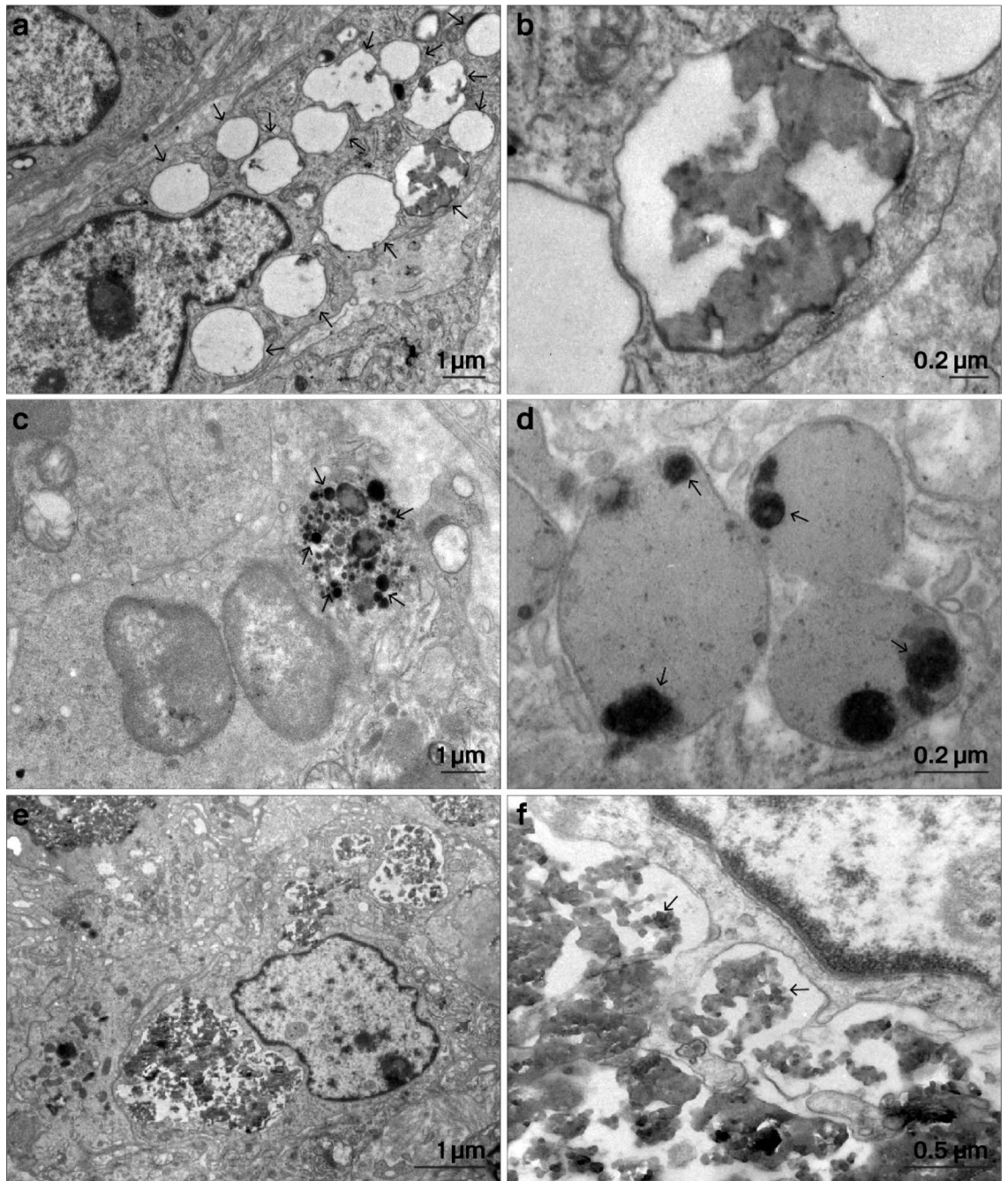


**Fig. 7.** Different types of particles phagocytosed by macrophages. (a, b) Microparticles (CE). (c, d) Nanoparticles (CS). (e, f) Non-encapsulated carbon nanoparticles (C-NPs).

In the TATTOO multicentric clinical study, lymph nodes were tattooed with 3 ml of Spot<sup>®</sup> commercial carbon suspension or 0.6 ml of CARBO-REP<sup>®</sup>. They found 83.6% of the lymph nodes<sup>22</sup>. Goyal et al.<sup>24</sup> tattooed the SLN with 2 ml of Spot<sup>®</sup> or Black Eye<sup>®</sup> reporting an intraoperative identification of 75–82%. Natsiopoulou et al.<sup>18</sup> successfully identified 93.3% of nodes injected with 0.3–0.7 ml of Spot<sup>®</sup>. Allweis et al.<sup>20</sup> injected by ultrasound guidance 0.2–0.5 ml doses of Spot<sup>®</sup> with an identification rate of 95%. Patel et al.<sup>21</sup> reported a 100% identification rate after injection of 0.1–1 ml Spot<sup>®</sup>. Dostalek et al.<sup>25</sup> tattooed with 0.1–0.5 ml of an activated carbon dispersion (Carbosorb, IMUNA PHARM, Slovakia) reporting an intraoperative detection rate of 81%. Kim et al.<sup>41</sup> reported a 98% detection rate using activated charcoal (Charcotrace<sup>™</sup>). Choy et al.<sup>42</sup> used 0.1–0.5 ml of Spot<sup>®</sup> to tattoo the nodes with an identification rate of 93.7–94.6%. Park et al.<sup>19</sup> tattooed the nodes with 0.5 ml of Spot<sup>®</sup> reporting an identification rate of SLN of 100%. In another recent clinical trial (NEOTARGET), 69% of carbon tattooed nodes (Sterimark<sup>®</sup>) were optimally localized intraoperatively<sup>23</sup>.

In the present study we explored the effect of factors such as time (1 to 16 weeks), particle size (range ~100 nm and ~1 μm) and concentration (10 and 20 mg/ml), on the tattooing of the lymph nodes and the tissue reaction.

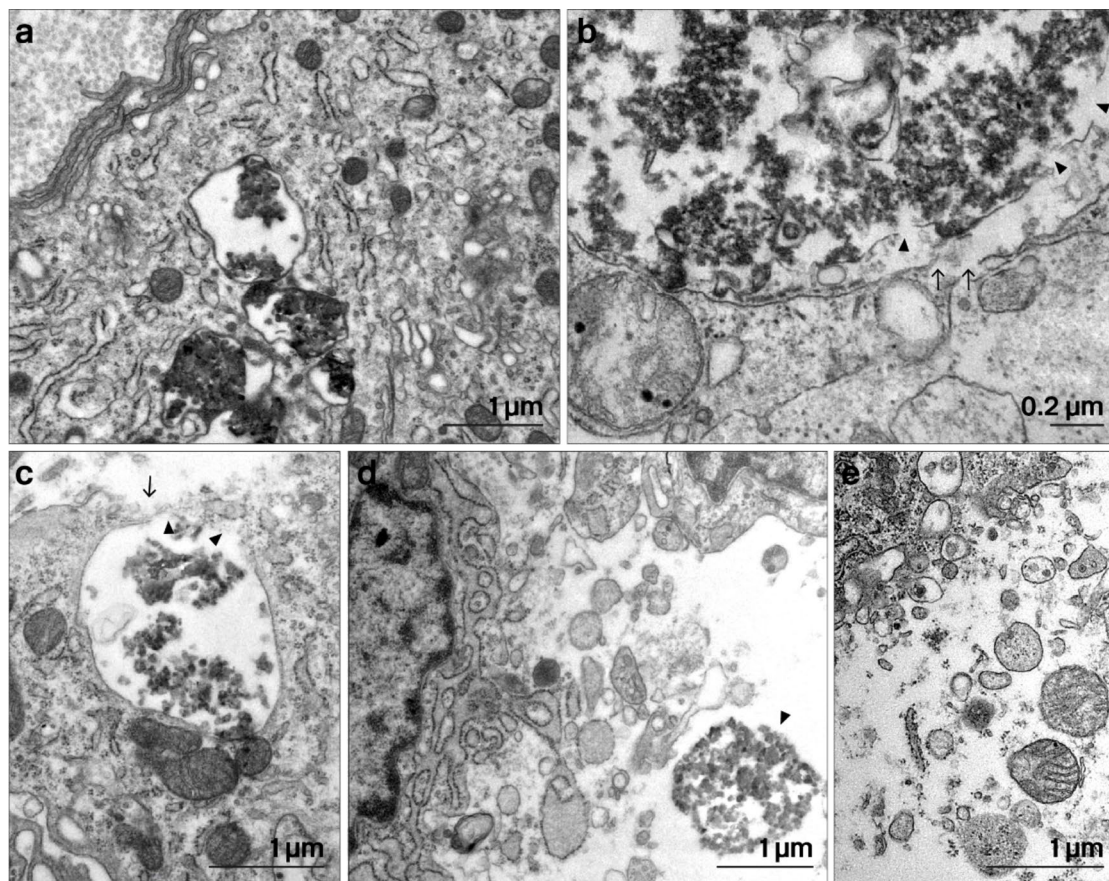


**Fig. 8.** Effect of particles on macrophages. (a) Detail of the cytoplasm of a macrophage showing lysosomes with carbon particles (C-NPs) inside. (b) Carbon particles rupture the membrane of phagolysosomes (arrowheads), releasing lysosomal hydrolases that rupture the cell plasma membrane (arrows). (c) Plasma membrane of a macrophage lysed by spilled hydrolases. The rupture of the phagosome membrane (arrowheads) and the plasma membrane (arrows) is observed. (d) After rupture of the plasma membrane, the carbon particles remain intact in the extracellular medium. (e) The organelles spilled into the extracellular space preserve their structure.

Studies on tissue response in the different time periods after injection of carbon-based markers are scarce. The cytotoxicity of carbon nanostructures is still a matter of debate. Although some authors report that carbon particles are inert and non-cytotoxic, others reported inflammatory reactions to varied degrees<sup>43–46</sup>. In our study, all tattoos tested in this work induced foreign body inflammatory reactions. This type of inflammation is normal after the inoculation of nano- and micro-particles into the body as previously reported<sup>47</sup>. We demonstrate that the pigment particles remaining in the lymph node or in the adjacent soft tissue are mainly located within inflammatory tissue. As time goes by, the inflammatory reaction decreases and the intensity of the tattooing also decreases.

Some preclinical studies revealed the diffusion of carbon-based particles to extranodal lymphoid tissue in 10.7–13.0% of cases<sup>18,24,42</sup>, probably because of the small size of the carbon particles. It is also observed greater dissemination of the tattooing as the time between tattooing and surgery increased<sup>24</sup>. In this work, the statistical studies do not conclude an evident correlation between the adjacent location of the particles and the stabling time of the animals. However, some lymph nodes could not be identified in the lymph node dissection surgery. Therefore, these non-tattooed lymph nodes could have lost the tattooing by dissemination to adjacent tissue and this study may underestimate this possibility.

The effect of particle size affects particle biodistribution. In the lymph node, inoculation of particles with a size > 100 nm is recommended to maximize stability and persistence<sup>48–50</sup>. However, nanoparticles < 10 nm can easily enter the capillaries and are quickly eliminated after injection<sup>51,52</sup>. Xu et al.<sup>53</sup> demonstrated that 50, 200 and 500 nm NPs migrate effectively to tumour-draining lymph nodes, although the efficiency of NPs accumulation in the nodes was negatively correlated with the size of the NPs. In other studies, PLGA NPs with a diameter > 1 µm have been reported to have lower uptake in the lymph node than NPs with a diameter of 300 nm<sup>54,55</sup>. This has been attributed to the fact that macrophages show a greater capacity to phagocytose nanoparticles than microparticles<sup>53</sup>. We synthesized nanoparticles (by emulsion, CS) in the ~100 nm range, and microparticles (electrosprayed, CE) in the ~1 µm range to study the effect of particle size. For both particles, the final ratio between PLGA and C-NPs loaded was very similar, so variations in the biological effects were

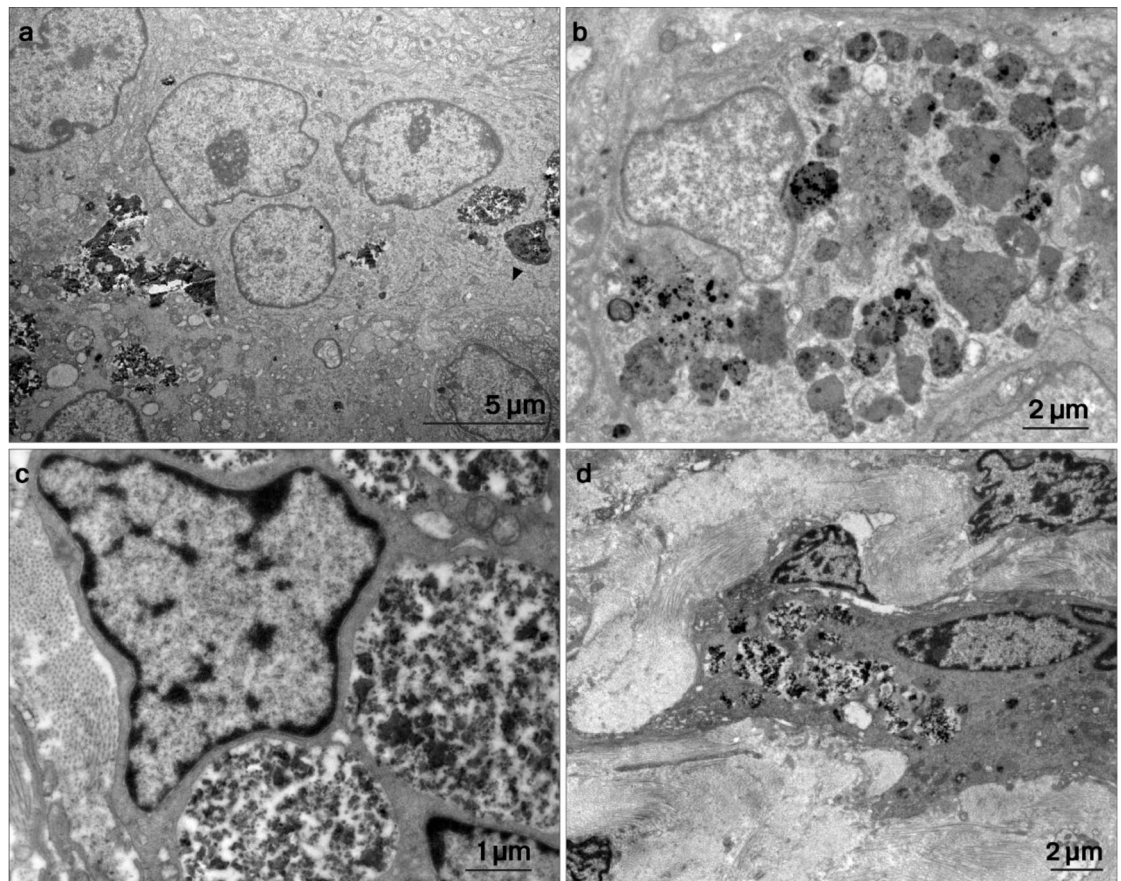


**Fig. 9.** Particle isolation in GMC and particle interaction with macrophages in the long term. **(a)** Carbon particles (C-NPs) internalized in a GMC. **(b)** Highly particle-laden macrophage (after 16 weeks). **(c)** The polymer of CS and CE particles is degraded, and free C-NPs appear inside macrophages. **(d)** Particle-laden macrophage is isolated within a matrix of collagen fibers.

associated with particle size. Lymph nodes tattooed with larger particle sizes (CE) showed easier identification than smaller particles (CS) did. The tattooed areas were similar in CE and CS-tattooed lymph nodes. According to other studies<sup>53</sup>, this phenomenon may be because microparticles are phagocytosed to a lesser extent and are better preserved in the lymph node. We also found that particle size had a significant effect on the intensity of the inflammatory reaction, with inflammation increasing with particle size. This could be associated with a higher amount of carbon in these particles and reduced phagocytosis of the microparticles<sup>53</sup>, leading to increased immune activity to deal with the particles. Nonencapsulated C-NPs show large inflammatory reactions and increased breakdown of macrophage phagolysosomes (associated with free C-NPs), leading to a higher rate of cell death according with our ultrastructural studies. These experimental results were like those obtained in the *in vitro* cytotoxicity assays, where we found that polymer-encapsulated C-NPs reduce carbon toxicity<sup>56</sup>.

The concentration of particles was explored at 10 and 20 mg/ml, only effects on the identification rates were observed. The identification rate was higher in CE20 and CS20 nodes with respect to CE10 and CS10, respectively. Additionally, CE20 significantly improved the identification of lymph nodes compared to CE10. In CS samples, no statically significant conclusions were observed. In contrast, other authors suggest that the administered volume (and, therefore, final particle concentration) does not correlate with ease of identification<sup>24</sup>.

The biological effect of tattooing lymph nodes with (nonencapsulated) carbon particles remains deeply unknown. Using transmission electron microscopy, we were able to observe the interaction of the particles with macrophages (Fig. 10). We observed a dynamic process in which phagocytosed particles were released to the extracellular medium and re-uptaken by new macrophages as part of a detoxification process. We found that particles were phagocytosed or isolated in GMC from the first week. Phagocytosis of exogenous particles by macrophages is one of the main mechanisms of innate immune defense<sup>57–59</sup>. Although particles were mainly found in macrophages, large amounts of particles were also observed inside GMC. GMC formation associated with foreign bodies (typically between 10 and 100  $\mu\text{m}$ ) is a frequent phenomenon<sup>60,61</sup>. This is in accordance with previous studies in skin which demonstrate that dermal macrophages constitute the primary store of dermal tattoo pigment in mice<sup>62</sup>.

An important aspect before progressing to clinical trials is to ensure that carbon-based tattoos do not affect the pathological examination of the nodal tissue. However, in other studies pathologists did not consider histologic evaluation to be complicated by the carbonaceous pigment<sup>18,19,21,22</sup>.

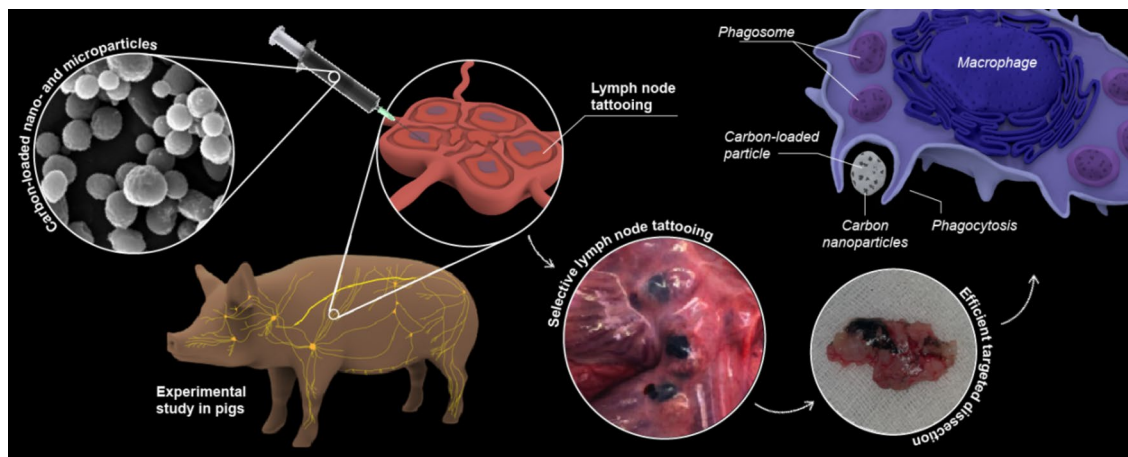


**Fig. 10.** Overview of the lymph node tattooing technique and its biological effect on the lymph node. Created with Sciency<sup>7</sup>.

In this preliminary study, all included variables showed greater efficiency for the synthesized particles compared to the control tattoos (nonencapsulated C-NPs). In week 1, the inflammation produced by the nonencapsulated carbon was more than double than that of the polymer-encapsulated carbon. Moreover, in the long-term study group, no C-NPs-tattooed lymph nodes were easily identified. We could not detect nodes tattooed with C-NPs after long periods of stabling (from 6 weeks onwards). Therefore, the encapsulation of C-NPs in polymeric systems improves the efficiency when tattooing nodes.

In vitro release studies showed very slow-release rates of C-NPs from the polymeric systems chosen. However, the degradation pattern of the polymers varies as a function of the pH of the medium<sup>63</sup>. The lysosomal pH is estimated to be between 4.5 and 5, which accelerates PLGA degradation<sup>63,64</sup>. Under recreated lysosomal conditions, PLGA degradation was estimated to be close to ~40% after 4 weeks<sup>65</sup>. These in vitro results could explain the higher release rate of C-NPs in our in vivo studies since we found free C-NPs as early as 4 weeks after inoculation. Our results are in agreement with previous studies which have shown a faster PLGA degradation rate in vivo compared to in vitro attributed to an autocatalytic effect of the acidic hydrolyzed byproducts<sup>66</sup>.

At clinical level, ease of identification and a reduced inflammatory reaction are the most relevant variables to grant subsequent clinical development. On the one hand, our preliminary results indicate that polymer-encapsulated C-NPs smaller in size (nano over micron) show lower inflammatory reaction. In this sense, the use of polymers with larger periods of degradation could reduce the inflammation due to the lower release of C-NPs. On the other hand, polymer-encapsulated C-NPs greater in size (micron over nano) lightly improved the ease of identification. In general, thanks to the polymer encapsulation the inflammatory reaction caused by the C-based nanomaterials highly decreases and the initial inflammation decreases over time showing no signs after 16 weeks. No fibrotic tissue was detected either. Therefore, polymer encapsulation of C-NPs currently used in clinical trials is beneficial for SLN tattooing. Future studies will be conducted using a larger animal sample to verify our findings always taking into account the principles of the 3Rs (Replacement, Refinement and Reduction).

## Conclusion

In order to facilitate SLN identification during surgery we have proposed the use of polymer encapsulated carbon-based nanoparticles to reduce unwanted bare nanoparticles migration and to control their local release and cellular uptake. In doing so, we have demonstrated in a preclinical study that it is possible to clearly identify by the naked eye tattooed mesenteric lymph nodes even 16 weeks after labelling. Of all the particles tested in this preliminary study, CS20 and CE20 tattooing showed similar reduction in the thickness of the inflammatory tissue (~2.1 and ~1.5-fold, respectively). Likewise, the reduction of the tattooed area was ~1.9-fold (CS20), and ~2.2-fold reduction (CE20) from short-term to long-term study groups, respectively. After 16 weeks of stabling, the presence of an inflammatory response was substantially reduced and almost all lymph nodes labelled showed mild or no inflammation. CE20 showed superior positive identification rates (100%) and similar tattooed areas than the others vectors tested. Therefore, it represents the most efficient tattooing of the lymph node compared to the other vectors studied. However, further studies are required to confirm these findings.

## Data availability

All data generated or analyzed during this study are included in this published article and its supplementary information file.

Received: 3 September 2024; Accepted: 22 November 2024

Published online: 27 November 2024

## References

- Turner, R., Olilla, D., Krasne, D. & Giuliano, A. Histopathologic validation of the Sentinel Lymph Node hypothesis for breast carcinoma. *Ann. Surg.* **226**, 271–276 (1997).
- Giuliano, A., Kirgan, D., Guenther, J. & Morton, D. Lymphatic mapping and Sentinel Lymphadenectomy for breast Cancer. *Ann. Surg.* **220**, 391–398 (1994).
- Boughey, J. et al. Sentinel Node surgery after Neoadjuvant Chemotherapy in patients with node-positive breast Cancer: the American College of Surgeons Oncology Group. Z1071 clinical trial. *JAMA* **310**, 1455–1461 (2013).
- Kuehn, T. et al. Sentinel-Lymph-Node Biopsy in patients with breast Cancer before and after Neoadjuvant Chemotherapy (SENTINA): a prospective, Multicenter Cohort Study. *Lancet Oncol.* **14**, 608–618 (2013).
- Boileau, J. et al. Sentinel Node Biopsy after Neoadjuvant Chemotherapy in Biopsy-Proven node-positive breast Cancer: the SN FNAC Study. *J. Clin. Oncol.* **20**, 2588–2564 (2015).
- Cao, S. et al. Feasibility and Reliability of Sentinel Lymph Node Biopsy after Neoadjuvant Chemotherapy in breast Cancer patients with positive axillary nodes at initial diagnosis: an up-to-date Meta-analysis of 3,578 patients. *Breast* **59**, 256–269. <https://doi.org/10.1016/j.breast.2021.07.015> (2021).
- Plecha, D., Bai, S., Patterson, H., Thompson, C. & Shenk, R. Improving the Accuracy of Axillary Lymph Node surgery in breast Cancer with Ultrasound-guided wire localization of Biopsy Proven Metastatic Lymph Nodes. *Breast Oncol.* **22**, 4241–4246 (2015).
- Man, V. & Kwong, A. Different strategies in marking Axillary Lymph nodes in breast Cancer patients undergoing Neoadjuvant Medical treatment: a systematic review. *Breast Cancer Res. Treat.* **186**, 607–615. <https://doi.org/10.1007/s10549-021-06118-6> (2021).
- Kuemmel, S. et al. A prospective, Multicenter Registry Study to evaluate the clinical feasibility of targeted Axillary Dissection (TAD) in node-positive breast Cancer patients. *Ann. Surg.* **276**, e553–e562. <https://doi.org/10.1097/SLA.0000000000004572> (2022).
- Greenwood, H. I., Wong, J. M., Mukhtar, R. A., Alvarado, M. D. & Price, E. R. Feasibility of magnetic seeds for preoperative localization of Axillary Lymph nodes in breast Cancer Treatment. *Am. J. Roentgenol.* **213**, 953–957. <https://doi.org/10.2214/AJR.19.21378> (2019).
- Martínez, M. et al. Evaluation of Axillary Lymph Node Marking with Magseed<sup>®</sup> before and after Neoadjuvant Systemic Therapy in Breast Cancer Patients: MAGNET Study. *Breast J.* (2022). <https://doi.org/10.1155/2022/6111907>
- Straver, M. E., Loo, C. E., Alderliesten, T., Rutgers, E. J. T. & Vrancken Peeters M.T.F.D. marking the Axilla with Radioactive Iodine seeds (MARI Procedure) May reduce the need for Axillary dissection after neoadjuvant chemotherapy for breast Cancer. *Br. J. Surg.* **97**, 1226–1231. <https://doi.org/10.1002/bjs.7073> (2010).
- Donker, M. et al. T.F.D. marking Axillary Lymph Nodes with Radioactive Iodine seeds for Axillary staging after neoadjuvant systemic treatment in breast Cancer patients. *Ann. Surg.* **261**, 378–382. <https://doi.org/10.1097/SLA.0000000000000558> (2015).
- Caudle, A. S. et al. Improved axillary evaluation following neoadjuvant therapy for patients with node-positive breast Cancer using selective evaluation of clipped nodes: implementation of targeted Axillary Dissection. *J. Clin. Oncol.* **34**, 1072–1078. <https://doi.org/10.1200/JCO.2015.64.0094> (2016).
- Falcon, S., Weinfurter, R. J., Mooney, B. & Niell, B. L. SAVI SCOUT<sup>®</sup> localization of breast lesions as a practical alternative to wires: outcomes and suggestions for trouble-shooting. *Clin. Imaging.* **52**, 280–286. <https://doi.org/10.1016/j.clinimag.2018.07.008> (2018).
- Sun, J. et al. Feasibility of Axillary Lymph Node localization and excision using Radar Reflector localization. *Clin. Breast Cancer.* **21**, e189–e193. <https://doi.org/10.1016/j.clbc.2020.08.001> (2021).
- Choy, N. et al. Initial results with preoperative tattooing of Biopsied Axillary Lymph nodes and correlation to Sentinel Lymph nodes in breast Cancer patients. *Ann. Surg. Oncol.* **22**, 377–382 (2015).
- Natsiopoulos, I. et al. Axillary Lymph Node Tattooing and targeted axillary dissection in breast Cancer patients who presented as CN + before Neoadjuvant Chemotherapy and Became CN0 after treatment. *Clin. Breast Cancer.* **19**, 208–215. <https://doi.org/10.1016/j.clbc.2019.01.013> (2019).
- Park, S. et al. Feasibility of Charcoal Tattooing of Cytology-Proven metastatic axillary lymph node at diagnosis and Sentinel Lymph Node Biopsy after Neoadjuvant Chemotherapy in breast Cancer patients. *Cancer Res. Treat.* **50**, 801–812. <https://doi.org/10.4143/crt.2017.210> (2018).
- Allweis, T. M. et al. Ultrasound guided tattooing of Axillary Lymph nodes in breast Cancer patients prior to Neoadjuvant Therapy, and identification of Tattooed Nodes at the time of surgery. *Eur. J. Surg. Oncol.* **46**, 1041–1045. <https://doi.org/10.1016/j.ejso.2019.11.501> (2020).
- Patel, R. et al. Pretreatment tattoo marking of suspicious Axillary Lymph nodes: reliability and correlation with Sentinel Lymph Node. *Ann. Surg. Oncol.* **26**, 2452–2458. <https://doi.org/10.1245/s10434-019-07419-3> (2019).
- Hartmann, S. et al. Carbon Tattooing for targeted Lymph Node Biopsy after primary systemic therapy in breast Cancer: prospective Multicentre TATTOO trial. *Br. J. Surg.* **108**, 302–307. <https://doi.org/10.1093/bjs/znaa083> (2021).
- Pinto, D. et al. Targeted Axillary Dissection after Chemotherapy: feasibility study with clip and Carbon Dye tattoo – neotarget trial. *Breast Care.* **17**, 166–171. <https://doi.org/10.1159/000517208> (2022).
- Goyal, A. et al. A Multicentre prospective feasibility study of Carbon Dye Tattooing of Biopsied Axillary Node and Surgical localisation in breast Cancer patients. *Breast Cancer Res. Treat.* **185**, 433–440. <https://doi.org/10.1007/s10549-020-05961-3> (2021).
- Dostalek, L., Cerny, A., Saskova, P. & Pavlista, D. Selective extirpation of Tattooed Lymph Node in Combination with Sentinel Lymph Node Biopsy in the management of node-positive breast Cancer patients after Neoadjuvant systemic therapy. *Breast Care.* **16**, 623–629. <https://doi.org/10.1159/000514266> (2021).
- Li, J. et al. Long-term tracing and staining of Carbon nanoparticles for Axillary Lymph nodes in patients with locally advanced breast Cancer treated with Neoadjuvant Chemotherapy. *Asian J. Surg.* **45**, 89–96. <https://doi.org/10.1016/j.asjsur.2021.03.020> (2022).
- Gatek, J. et al. Targeted Axillary dissection with preoperative tattooing of Biopsied positive axillary lymph nodes in breast Cancer. *Neoplasma* **67**, 1329–1334 (2020).
- Martínez, G. et al. Use of a Polyol Liquid Collection Medium to obtain Ultrasmall magnetic nanoparticles by laser pyrolysis. *Nanotechnology* **23**, 425605. <https://doi.org/10.1088/0957-4484/23/42/425605> (2012).
- Mas, N. et al. Laser-driven direct synthesis of Carbon Nanodots and Application as Sensitizers for Visible-Light Photocatalysis. *Carbon N Y.* **156**, 453–462. <https://doi.org/10.1016/j.carbon.2019.09.073> (2020).
- Arruebo, M. et al. Continuous synthesis of drug-loaded nanoparticles using Microchannel Emulsification and Numerical modeling: Effect of Passive Mixing. *Int. J. Nanomed.* **Volume 11**, 3397–3416. <https://doi.org/10.2147/IJN.S108812> (2016).
- Gámez-Herrera, E. et al. Drug-eluting wound dressings having sustained release of Antimicrobial compounds. *Eur. J. Pharm. Biopharm.* **152**, 327–339. <https://doi.org/10.1016/j.ejpb.2020.05.025> (2020).
- Kim, M. H., Kim, B. S., Park, H., Lee, J. & Park, W. H. Injectable Methylcellulose Hydrogel Containing Calcium Phosphate Nanoparticles for bone regeneration. *Int. J. Biol. Macromol.* **109**, 57–64. <https://doi.org/10.1016/j.ijbiomac.2017.12.068> (2018).
- Xia, H., Wang, Q. & Qiu, G. Polymer-encapsulated Carbon nanotubes prepared through ultrasonically initiated in situ emulsion polymerization. *Chem. Mater.* **15**, 3879–3886. <https://doi.org/10.1021/cm0341890> (2003).
- Jäger, C., Henning, T., Schlögl, R. & Spillecke, O. Spectral Properties of Carbon Black. *J. Non Cryst. Solids.* **258**, 161–179. [https://doi.org/10.1016/S0022-3093\(99\)00436-6](https://doi.org/10.1016/S0022-3093(99)00436-6) (1999).
- Abnova, B. Cell Viability Assay Kit.

36. Schindelin, J. et al. Fiji: an Open-Source platform for Biological-Image analysis. *Nat. Methods*. **9**, 676–682. <https://doi.org/10.1038/nmeth.2019> (2012).
37. Hoseini, B. et al. Application of Ensemble Machine Learning Approach to assess the factors affecting size and Polydispersity Index of Liposomal Nanoparticles. *Sci. Rep.* **13**, 18012. <https://doi.org/10.1038/s41598-023-43689-4> (2023).
38. Youshia, J., Ali, M. E. & Lamprecht, A. Artificial neural network based particle size prediction of polymeric nanoparticles. *Eur. J. Pharm. Biopharm.* **119**, 333–342. <https://doi.org/10.1016/j.ejpb.2017.06.030> (2017).
39. ISO 10993-5. Biological evaluation of Medical devices (part 5: tests (2009). for in Vitro Cytotoxicity).
40. Banys-Paluchowski, M. et al. Axillary Ultrasound for Prediction of response to Neoadjuvant Therapy in the Context of Surgical strategies to Axillary Dissection in primary breast Cancer: a systematic review of the current literature. *Arch. Gynecol. Obstet.* **301**, 341–353. <https://doi.org/10.1007/s00404-019-05428-x> (2020).
41. Kim, W. H. et al. Ultrasound-guided restaging and localization of Axillary Lymph nodes after Neoadjuvant Chemotherapy for Guidance of Axillary surgery in breast Cancer patients: experience with activated Charcoal. *Ann. Surg. Oncol.* **25**, 494–500. <https://doi.org/10.1245/s10434-017-6250-3> (2018).
42. Choy, N. et al. Initial results with preoperative tattooing of Biopsied Axillary Lymph nodes and correlation to Sentinel Lymph nodes in breast Cancer patients. *Ann. Surg. Oncol.* **22**, 377–382. <https://doi.org/10.1245/s10434-014-4034-6> (2015).
43. Xie, P., Yang, S. S. T., He, T., Yang, S. S. T. & Tang, X. H. Bioaccumulation and Toxicity of Carbon nanoparticles suspension injection in Intravenously exposed mice. *Int. J. Mol. Sci.* **18** <https://doi.org/10.3390/ijms18122562> (2017).
44. Chang, X. L., Yang, S. T. & Xing, G. Molecular Toxicity of nanomaterials. *J. Biomed. Nanotechnol.* **10**, 2828–2851. <https://doi.org/10.1166/jbn.2014.1936> (2014).
45. Liu, J. H. et al. Biocompatibility of Graphene Oxide Intravenously Administrated in mice—effects of Dose, size and exposure protocols. *Toxicol. Res. (Camb)*. **4**, 83–91. <https://doi.org/10.1039/C4TX00044G> (2015).
46. Duch, M. C. et al. Minimizing oxidation and stable Nanoscale Dispersion improves the biocompatibility of Graphene in the lung. *Nano Lett.* **11**, 5201–5207. <https://doi.org/10.1021/nl202515a> (2011).
47. Ernst, L., Casals, E., Italiani, P., Boraschi, D. & Puentes, V. The interactions between nanoparticles and the Innate Immune System from a nanotechnologist perspective. *Nanomaterials* **11**, 2991. <https://doi.org/10.3390/nano11112991> (2021).
48. Mariani, G. et al. Radioguided Sentinel Lymph Node Biopsy in breast Cancer surgery. *J. Nucl. Med.* **42**, 1198–1215 (2001).
49. Ahmed, M. et al. Optimising magnetic Sentinel Lymph Node Biopsy in an in vivo Porcine Model. *Nanomed. Nanotechnol. Biol. Med.* **11**, 993–1002. <https://doi.org/10.1016/j.nano.2015.01.010> (2015).
50. Liu, J., Scollard, D. A., Reilly, R. M., Wu, X. Y. & Johnston, M. R. Effect of particle size on the lymphatic distribution of <sup>111</sup>Indium-Aminopolystyrene through Intrapleural Administration. *Lymphology* **41**, 153–160 (2008).
51. Rohner, N. A. & Thomas, S. N. Flexible macromolecule versus rigid particle Retention in the injected skin and Accumulation in draining Lymph Nodes are differentially influenced by hydrodynamic size. *ACS Biomater. Sci. Eng.* **3**, 153–159. <https://doi.org/10.1021/acsbomaterials.6b00438> (2017).
52. Wang, Y. et al. Effect of Physicochemical Properties on in vivo fate of nanoparticle-based Cancer immunotherapies. *Acta Pharm. Sin B*. **11**, 886–902. <https://doi.org/10.1016/j.apsb.2021.03.007> (2021).
53. Xu, J. et al. Yeast-derived nanoparticles remodel the Immunosuppressive Microenvironment in Tumor and Tumor-Draining Lymph nodes to suppress Tumor Growth. *Nat. Commun.* <https://doi.org/10.1038/s41467-021-27750-2> (2022).
54. Jia, J. et al. Interactions between nanoparticles and dendritic cells: from the perspective of Cancer Immunotherapy. *Front. Oncol.* <https://doi.org/10.3389/fonc.2018.00404> (2018).
55. Joshi, V. B., Geary, S. M. & Salem, A. K. Biodegradable particles as Vaccine Delivery systems: size matters. *AAPS J.* **15**, 85–94. <https://doi.org/10.1208/s12248-012-9418-6> (2013).
56. Hung, H. I. et al. PLGA nanoparticle encapsulation reduces toxicity while retaining the therapeutic efficacy of EtNBS-PDT in Vitro. *Sci. Rep.* <https://doi.org/10.1038/srep33234> (2016).
57. Donahue, N. D., Acar, H. & Wilhelm, S. Concepts of Nanoparticle Cellular Uptake, intracellular trafficking, and kinetics in Nanomedicine. *Adv. Drug Deliv. Rev.* **143**, 68–96. <https://doi.org/10.1016/j.addr.2019.04.008> (2019).
58. Juliano, R. L. Factors affecting the Clearance Kinetics and Tissue Distribution of Liposomes, microspheres and emulsions. *Adv. Drug Deliv. Rev.* **2**, 31–54. [https://doi.org/10.1016/0169-409X\(88\)90004-X](https://doi.org/10.1016/0169-409X(88)90004-X) (1988).
59. Hillaireau, H. & Couvreur, P. Nanocarriers' entry into the cell: relevance to drug delivery. *Cell. Mol. Life Sci.* **66**, 2873–2896. <https://doi.org/10.1007/s00018-009-0053-z> (2009).
60. Kang, M. S. et al. Uptake and toxicity of Cerium Dioxide nanoparticles with different aspect ratio. *Toxicol. Lett.* **373**, 196–209. <https://doi.org/10.1016/j.toxlet.2022.11.013> (2023).
61. Herde, K. et al. Connexin 43 expression of Foreign Body Giant cells after implantation of Nanoparticulate Hydroxyapatite. *Biomaterials* **28**, 4912–4921. <https://doi.org/10.1016/j.biomaterials.2007.07.027> (2007).
62. Baranska, A. et al. Unveiling skin Macrophage Dynamics explains both tattoo persistence and strenuous removal. *J. Exp. Med.* **215**, 1115–1133. <https://doi.org/10.1084/jem.20171608> (2018).
63. Zolnik, B. S. & Burgess, D. J. Effect of Acidic PH on PLGA Microsphere Degradation and Release. *J. Control Release.* **122**, 338–344. <https://doi.org/10.1016/j.jconrel.2007.05.034> (2007).
64. Chen, R., Jäättelä, M. & Liu, B. Lysosome as a Central Hub for Rewiring PH Homeostasis in Tumors. *Cancers (Basel)*. **12**, 2437. <https://doi.org/10.3390/cancers12092437> (2020).
65. del Moral, M. et al. Role of the Lactide:glycolide ratio in PLGA Nanoparticle Stability and Release under Lysosomal Conditions for Enzyme Replacement Therapy of Lysosomal Storage Disorders. *J. Funct. Biomater.* **14**, 440. <https://doi.org/10.3390/jfb14090440> (2023).
66. Lu, L. et al. A.G. In Vitro and in Vivo Degradation of Porous Poly(DL-Lactic-Co-Glycolic Acid) Foams. *Biomaterials*. (2000). [https://doi.org/10.1016/S0142-9612\(00\)00047-8](https://doi.org/10.1016/S0142-9612(00)00047-8)

## Acknowledgements

Authors would like to acknowledge the use of “Servicio General de Apoyo a la Investigación (SAI)” from the University of Zaragoza (Zaragoza, Spain), and the use of “Servicio de Microscopía Electrónica” from the “Centro de Investigación Príncipe Felipe” (Valencia, Spain). G.M. gratefully acknowledges the support from the Miguel Servet Program (MS19/00092; ISCIII).

## Author contributions

Conceptualization, A.G., M.A., M.B.; Synthesis and characterization: M.B., C.Y., T.A.; Surgery procedures: A.G., M.B. and D.A.; Histological studies: E.M., and M.B.; Electron-microscopy investigation, C.J., and M.B.; Statistical analysis: M.B.; Writing – Original Draft, M.B., E.M.; Writing – Review & Editing, A.G., M.A., V.S., C.Y., C.J., D.A., G.M.; T.A.; Supervision, A.G., M.A., E.M., C.J.

### Funding

This work was supported by the Instituto de Salud Carlos III (ISCIII) [DTS20/00131].

### Declarations

#### Ethics approval and consent to participate

This research was approved by the Animal Research Ethics Committee of the University of Zaragoza under reference PI09/20.

#### Competing interests

The authors declare no competing interests.

#### Additional information

**Supplementary Information** The online version contains supplementary material available at <https://doi.org/10.1038/s41598-024-80931-z>.

**Correspondence** and requests for materials should be addressed to C.Y.

**Reprints and permissions information** is available at [www.nature.com/reprints](http://www.nature.com/reprints).

**Publisher's note** Springer Nature remains neutral with regard to jurisdictional claims in published maps and institutional affiliations.

**Open Access** This article is licensed under a Creative Commons Attribution-NonCommercial-NoDerivatives 4.0 International License, which permits any non-commercial use, sharing, distribution and reproduction in any medium or format, as long as you give appropriate credit to the original author(s) and the source, provide a link to the Creative Commons licence, and indicate if you modified the licensed material. You do not have permission under this licence to share adapted material derived from this article or parts of it. The images or other third party material in this article are included in the article's Creative Commons licence, unless indicated otherwise in a credit line to the material. If material is not included in the article's Creative Commons licence and your intended use is not permitted by statutory regulation or exceeds the permitted use, you will need to obtain permission directly from the copyright holder. To view a copy of this licence, visit <http://creativecommons.org/licenses/by-nc-nd/4.0/>.

© The Author(s) 2024